Research Article

Title: **A functional topography within the cholinergic basal forebrain for processing sensory cues associated with reward and punishment**

Author names and affiliations: Blaise Robert[1], Eyal Y. Kimchi[1,2], Yurika Watanabe[1], Tatenda Chakoma[1], Miao Jing[3], Yulong Li[4], and Daniel B. Polley*[1,5]

1- Eaton-Peabody Laboratories, Massachusetts Eye and Ear Infirmary, Boston MA 02114 USA
2- Dept. Neurology, Massachusetts General Hospital, Boston MA 02114
3- Chinese Institute for Brain Research, Beijing 102206, China.
4- State Key Laboratory of Membrane Biology, Peking University School of Life Sciences; PKU-IDG/McGovern Institute for Brain Research; Peking-Tsinghua Center for Life Sciences, Beijing 100871, China
5- Dept. Otolaryngology - Head and Neck Surgery, Harvard Medical School, Boston MA 02114 USA

* Corresponding author and Lead Contact

*Correspondence: daniel_polley@meei.harvard.edu

Keywords: acetylcholine; cholinergic; basal forebrain; nucleus basalis; horizontal limb diagonal band; substantia innominata; reward; punishment; learning; auditory

Abstract

Basal forebrain cholinergic neurons (BFCNs) project throughout the cortex to regulate arousal, stimulus salience, plasticity, and learning. The basal forebrain features distinct connectivity along its anteroposterior axis that could impart regional differences in feature processing. Here, we simultaneously measured bulk BFCN activity from an anterior structure, the horizontal limb of the diagonal band (HDB), and from the posterior tail of the basal forebrain in globus pallidus and substantia innominata (GP/SI) over a 30-day period as mice learned a sensory reversal task. Although HDB and GP/SI responses were similar for many features, HDB more closely tracked fluctuations in pupil-indexed brain state and exhibited stronger responses to reward omission than to delivery of anticipated awards. In GP/SI, BFCNs were strongly activated by sound, and this response was further enhanced for punishment-predicting – but not reward-predicting – cues. These results identify a functional topography that diversifies cholinergic modulatory signals broadcast to downstream brain regions.

Introduction

Basal forebrain projections innervate the neocortex, hippocampus, and amygdala to regulate stimulus salience and global brain state across a wide range of timescales (for recent reviews see (Disney and Higley, 2020; Monosov, 2020; Sarter and Lustig, 2020). The basal forebrain is not a monolithic structure, but rather a constellation of discrete brain areas that feature distinct combinations of neurochemical cell types and distinct arrangements of afferent and efferent connections (Gielow and Zaborszky, 2017; Li et al., 2018; Rye et al., 1984; Zaborszky et al., 2012). Any single region of the basal forebrain is composed of glutamatergic, GABAergic, and cholinergic neurons, which generally share the same sources of input but can vary widely between cell types both in their downstream targeting and functional response properties (Do et al., 2016; Laszlovszky et al., 2020; Yang et al., 2017). As a whole, the basal forebrain is understood to contribute to learning, memory, attention, arousal, and neurodegenerative disease processes (Everitt and Robbins, 1997; Monosov, 2020; Zaborszky et al., 2012). However, the heterogeneity of cell types and projection targets have made it challenging to identify specific computations or specialized feature processing performed by “the” basal forebrain, underscoring the need for cell type-specific recordings from targeted regions in task-engaged animals.

Basal forebrain cholinergic neurons (BFCNs), though numerically the rarest major neurochemical class of basal forebrain neuron (Gritti et al., 2006), are by the far the most extensively studied. In rats and mice, where cholinergic neurons can be accessed for tracing, monitoring and manipulation with transgenic approaches, BFCNs exhibit distinct arrangements of afferent and efferent connections along the extended rostrocaudal axis (Gielow and Zaborszky, 2017). BFCNs in a rostral structure, such as the horizontal limb of the diagonal band of Broca (HDB) feature strong reciprocal connectivity with prefrontal cortex and lateral hypothalamus, with additional projections to entorhinal cortex, olfactory bulb, and pyriform cortex (Bloem et al., 2014; Gielow and Zaborszky, 2017; Li et al., 2018; Rye et al., 1984; Zaborszky et al., 2012) (**Figure 1a**). By contrast, BFCNs at the caudal tail of the basal

forebrain, at the intersection of globus pallidus and substantia innominata (GP/SI), receive strong inputs from the caudate putamen, the medial geniculate and posterior intrathalamic nuclei, and are the primary source of cholinergic input to the auditory cortex (ACtx), with comparatively weak projections to frontal cortical areas (Chavez and Zaborszky, 2017; Guo et al., 2019; Kamke et al., 2005; Rye et al., 1984; Zaborszky et al., 2012).

Although rostral and caudal BFCNs are wired into distinct anatomical networks, the suggestion is that they broadcast a relatively unified signal to downstream brain areas. The evidence for this conclusion primarily comes from two types of measurements. First, whether from HDB (~0.5 – 0.8 mm rostral to bregma in mouse), an intermediate caudal area such as nucleus basalis (~0.9 – 0.5 mm caudal to bregma), or the caudal extreme GP/SI (~1.5mm caudal to bregma), and whether documented with optogenetically targeted single BFCN unit spiking or population-based calcium signals, all studies have emphasized strong, short-latency responses to aversive stimuli such as air puffs or foot shock (HDB - (Hangya et al., 2015; Harrison et al., 2016; Laszlovszky et al., 2020; Sturgill et al., 2020); nucleus basalis - (Hangya et al., 2015; Laszlovszky et al., 2020; Letzkus et al., 2011); GP/SI - (Guo et al., 2019)). Second, cortical fluorescence imaging of genetically encoded acetylcholine (ACh) sensors or calcium signals in BFCN axons have demonstrated a strong correspondence between cholinergic activity and behavioral indices of global arousal, as determined from EEG markers, iso-luminous pupil diameter changes, and gross motor markers such as grooming or locomotion (ACh sensor imaging - (Lohani et al., 2020; Teles-Grilo Ruivo et al., 2017); Calcium imaging for HDB - (Harrison et al., 2016; Sturgill et al., 2020), nucleus basalis - (Reimer et al., 2016), GP/SI - (Nelson and Mooney, 2016)).

On the other hand, there are many differences and inconsistencies in the emerging BFCN literature, which could point towards interesting differences in the anatomical source of measured signals, or else could arise from differences in mouse lines, behavioral task designs, and measurement techniques. For example, auditory cue-evoked BFCN responses have been described as absent altogether (Hangya et al., 2015), observed only for reward-predictive sounds (Crouse et al., 2020; Harrison et al., 2016; Kuchibhotla et al., 2017; Parikh et al., 2007), or enhanced after auditory learning but present even for unconditioned stimuli (Guo et al., 2019). Similarly, behavioral accuracy in discrimination tasks have been classified from BFCN activity both preceding and following the auditory cue (Kuchibhotla et al., 2017; Parikh et al., 2007), only from the post-cue response period (Laszlovszky et al., 2020; Sturgill et al., 2020), or only from putative non-cholinergic cell types (Hangya et al., 2015; Lin and Nicolelis, 2008). Reward-evoked BFCN activity has been described as weak overall (Crouse et al., 2020; Harrison et al., 2016; Parikh et al., 2007) or rapid and quite strong, particularly for uncertain rewards (Hangya et al., 2015; Laszlovszky et al., 2020; Sturgill et al., 2020; Teles-Grilo Ruivo et al., 2017). Finally, the relationship between BFCN activity and movement is unclear, with some studies reporting strong recruitment by orofacial movements or locomotion occurring outside of a behavioral task (Harrison et al., 2016; Nelson and Mooney, 2016), strong only for movements that linked to reinforcement (Crouse et al., 2020), or absent, whether movements were linked to reinforcement or not (Hangya et al., 2015; Parikh et al., 2007).

To better understand whether there are regional functional specializations within the basal forebrain, we developed an approach to minimize inter-subject variation by testing all of the experimental features mentioned above in each individual mouse while making simultaneous fiber-based bulk GCaMP recordings from BFCNs in HDB and GP/SI. For some variables, we observed closely matched responses in rostral and caudal regions, suggesting a common output that would be broadcast to downstream brain regions: both HDB and GP/SI exhibited equivalently strong adaptation to sensory novelty and equivalently weak overall responses to unconditioned visual stimuli, anticipated rewards, and neither region exhibited evidence of learning-related enhancement of reward-predictive auditory cues. For other measures, we noted clear differences between BFCN activity in each region: HDB exhibited a comparatively strong association with pupil-indexed brain state, behavioral trial outcome, and with the omission of expected rewards. Although BFCNs in both regions showed strong responses to punishment, responses were larger in GP/SI, as were responses to orofacial movements, unconditioned auditory stimuli, and learning-related enhancement of punishment-predicting auditory cues. These findings identify a coarse functional topography within the cholinergic basal forebrain that can be interpreted in light of the distinct connectivity of each region and will motivate future hypotheses about the causal involvement of each region in brain function and behavior.

Results

To characterize regional specializations within the cholinergic basal forebrain across a wide range of task-related variables, we performed dual fiber imaging from HDB and GP/SI in the right hemisphere of Chat-Cre mice that were crossed to the GCaMP6f reporter line, Ai148 (**Figure 1B-C**). We confirmed that GCaMP expression was almost entirely restricted to cholinergic neurons within the HDB and GP/SI by immunolabeling regions near the end of the fiber tip for ChAT in a subset of implanted mice (N=4). ChAT- expressing GCaMP neurons were rare, amounting to just 95/1719 in HDB (5.5%) and 48/764 in GP/SI (6.3%) (**Figure 1D**). Therefore, at least for the two regions of the basal forebrain characterized here, our transgenic strategy was appropriate for long-term calcium imaging in cholinergic basal forebrain neurons.

Strong coherence between pupil-indexed arousal and cholinergic activity

Basal forebrain neurons have a well-established role in regulating global brain state (Buzsaki et al., 1988; Kim et al., 2015; Yang et al., 2017). The cholinergic basal forebrain, in particular, is a key regulator of neocortical excitability across sleep states as well as levels of vigilance during quiescent awake states (Buzsaki et al., 1988; Everitt and Robbins, 1997; McGinley et al., 2015a; Reimer et al., 2016; Teles-Grilo Ruivo et al., 2017). Under iso-luminous lighting conditions, pupil diameter provides a sensitive index of arousal and has been shown to co-vary with GCaMP activity measured in cholinergic basal forebrain axon fields within the neocortex (Nelson and Mooney, 2016; Reimer et al., 2016). Prior measurements were either made in ChAT-Cre × GCaMP reporter lines or via relatively large viral solution injection quantities (0.4 – 1 μL), which leaves unresolved the question of how the activity of cholinergic neurons in

specific regions of the basal forebrain corresponds to pupil-indexed arousal state. To address this point, we simultaneously monitored spontaneous pupil fluctuations alongside fiber-based GCaMP imaging from HDB and GP/SI. We observed a striking correspondence between spontaneous pupil dilations and slow fluctuations in GCaMP signal amplitudes in both regions of the basal forebrain (**Figure 1E**). GCaMP coherence with pupil fluctuations was significantly higher in HDB than GP/SI, where bulk calcium dynamics could account for as much as 80% of the variability in slow pupil changes (**Figure 1F**, statistical reporting provided in figure legends). The timing of correlated GCaMP transients and pupil dilations were similar across brain areas, where GCaMP signals led pupil dilations by approximately 0.7s (**Figure 1G**).

One of the underlying assumptions in our approach is that bulk calcium imaging from ChAT-Cre neurons in the basal forebrain is a useful way to measure the suprathreshold activity of local BFCNs and infer the timing of ACh release in downstream targets. For example, based on the correspondence between basal forebrain bulk GCaMP levels and pupil diameter, it would be reasonable to hypothesize that ACh levels also co-vary with pupil dilations with a similar coherence. HDB and GP/SI BFCNs both project to ACtx, although BFCN → ACtx projections are far more numerous in GP/SI than HDB (Chavez and Zaborszky, 2017; Guo et al., 2019; Kamke et al., 2005; Rye et al., 1984). To monitor ACh dynamics in ACtx related to pupil fluctuations, we expressed the genetically encoded ACh fluorescent sensor, $GRAB_{ACh}3.0$, (ACh3.0), in ACtx neurons and monitored fluorescence dynamic with tapered optical fibers (**Figure 1H**) (Jing et al., 2020; Pisano et al., 2019). As expected, coherence between ACtx ACh3.0 fluorescence and pupil fluctuations strongly resembled GCaMP coherence from GP/SI cell bodies, both in terms of the strong coherence with slow (< 0.1 Hz) changes in pupil diameter (**Figure 1I**) and in terms of timing, where ACh3.0 signal surges led pupil dilations by approximately 0.6s (**Figure 1J**). These findings validate our use of bulk fiber-based calcium imaging in the GCaMP reporter line as a useful way to monitor cholinergic basal forebrain activity and additionally demonstrate a strong correspondence between pupil-indexed arousal and activity surges in HDB and – to a lesser extent – GP/SI.

Encoding and habituation for auditory and visual stimuli in the cholinergic basal forebrain

Having confirmed that our dual fiber bulk GCaMP imaging approach could capture the expected relationship between pupil-indexed brain state and cortical ACh levels, we next tested regional variations in BFCN responses for unconditioned auditory and visual stimuli that had no explicit behavioral significance (**Figure 2A**). As illustrated in an example mouse, auditory spectrotemporal gratings elicited robust responses from GP/SI but not HDB, whereas drifting visual gratings evoked modest responses from both regions (**Figure 2B**). Quantification of visual- and sound-evoked responses across all mice (N=11) revealed relatively weak visually evoked responses that were limited to the highest stimulus contrast in both HDB (**Figure 2C**) and GP/SI (**Figure 2D**). Sound-evoked responses increased monotonically with sound intensity and were significantly greater overall compared to visually evoked responses, but this difference was primarily driven by GP/SI, where auditory inputs have the unusual distinction of eliciting strong, rapid responses prior to behavioral conditioning, as described

previously in optogenetically identified cholinergic neurons (Guo et al., 2019) and unidentified unit recordings (Chernyshev and Weinberger, 1998; Guo et al., 2019; Maho et al., 1995).

Spontaneous pupil dilations (Fig. 1) can reflect a heighted arousal state, but pupil dilations can also be elicited by sounds that are novel, emotionally evocative, or require heightened listening effort (Becket Ebitz and Moore, 2019; Zekveld et al., 2018). Along these lines, we observed large pupil dilations to the first presentation of an auditory spectrotemporal gratings, which then habituated to approximately 50% of their initial amplitude after one or two trials, presumably reflecting the loss of stimulus novelty (**Figure 2E**). Sound-evoked BFCN responses decayed in parallel with pupil responses, where responses decreased by approximately 30% after the first presentation before stabilizing at approximately 60% of the initial amplitude across subsequent presentations. Although the sound-evoked response amplitude was greater overall in GP/SI than HDB, the proportional decay with habituation was equivalent (**Figure 2F**). To control for the possibility that the progressive response decay reflected photobleaching of the sample or another source of measurement noise, we also quantified the amplitude of spontaneous GCaMP transients measured during the “nothing” trials in which neither an auditory nor visual stimuli were presented. The amplitude of spontaneous GCaMP transients was stable throughout the recording period, confirming that the reduced sensory-evoked GCaMP responses over the course of 20 blocks reflected habituation to stimulus novelty (**Figure 2G**).

BFCN cue responses co-vary with behavioral accuracy but not learned reward outcome

Whereas BFCN responses to neutral, unconditioned sensory stimuli vary by stimulus modality and region, several prior studies have described a progressive enhancement in BFCN responses to tones associated with reward (Crouse et al., 2020; Harrison et al., 2016; Kuchibhotla et al., 2017; Parikh et al., 2007). Apart from learning-related increases in cue-evoked responses, variations in baseline activity rates or cue-evoked responses amplitudes have also been clearly linked to behavioral performance accuracy in sensory detection and recognition tasks (Kuchibhotla et al., 2017; Laszlovszky et al., 2020; Parikh et al., 2007; Sturgill et al., 2020). To determine how BFCN activity dynamics related to appetitive learning and task performance, we conditioned mice to lick a delivery spout shortly following the onset of a tone to receive a sugar water reward (**Figure 3A**). To temporally separate the cue, operant motor response, and reinforcement timing, reward delayed until mice produced an extended, vigorous bout of licking (≥7 licks in 2.8s). Although the rates of procedural learning varied somewhat between mice (**Figure 3B**), all mice learned the task within a few sessions and either detected the tone to receive reward (hit) or failed to lick at all in response to the tone (miss), with very few instances of partial hits (>0 but < 7 licks in 2.8s) observed after the first few behavioral sessions (**Figure 3C**).

We contrasted BFCN activity on hit and miss trials and noted a clear difference, both in the pre-cue baseline activity and cue-evoked response in HDB (**Figure 3D**) and GP/SI (**Figure 3E**). Miss trials featured elevated pre-stimulus BFCN activity levels and reduced sound-evoked responses (**Figure 3F-G**), where the difference in baseline activity rates between hit and miss trials was greater overall in HDB than GP/SI (**Figure 3H**). We were surprised to observe that

cue-evoked responses were not enhanced later in training, when the cue-reward association was well-learned (Figure 3F-G). While cue-evoked responses were significantly attenuated on miss trials, response amplitudes were not significantly changed in either trial type or brain region as mice learned the association between the auditory cue and reward (**Fig. 3I**).

Movement-related activity in the cholinergic basal forebrain

To determine how orofacial movements related to licking recruited BFCN activity independent of sensory cues and reinforcement, we turned to lick events recorded during the inter-trial interval. Licking behavior during the inter-trial period ranged from spurious checks of the lickspout, composed of just one or two successive licks, all the way to the occasional presentation of the operant lick bout behavior (i.e., a false alarm). As illustrated in an example mouse, we noted a modest increase in BFCN activity beginning shortly after the onset of an intense lick bout in GP/SI and, to a lesser extent, HDB (**Figure 4A, left column**). We also observed an unexpected second increase in BFCN activity following the offset of the lick bout (**Figure 4A, right column**). BFCN response to the onset of licks increased monotonically across lick bout duration and, while fairly modest overall, were significantly greater in GP/SI than HDB (**Figure 4B**). By contrast, BFCN responses elicited at the offset of lick bouts were only observed in bouts of seven or more licks, the criterion for reward delivery had a tone been presented (**Figure 4C**). In GP/SI, we noted only a minimal response to the offset of ≥7 licks, which was not significantly greater than the response to shorter lick bouts. Unlike activity related to the onset of licking, the offset response was significantly greater in HDB than GP/SI and was only observed when ≥7 licks were produced (**Figure 4D-E**). One interpretation of these findings is that the mouse occasionally deployed the full operant lick behavior during the silent inter-trial interval in anticipation of reward. In this scenario, the scaling of lick onset and offset responses with lick duration could corroborate recent findings that BFCNs are more strongly recruited by motor actions that are expected to result in reward (Crouse et al., 2020), a possibility that we addressed in the next stage of behavioral experiments.

Recruitment of BFCN responses to punishment, reward, and reward omission

To address how behavioral reinforcement – and the omission of anticipated reinforcement – recruited activity in different regions of the BFCN, mice were advanced to the next stage of the operant training procedure, in which one of the tone frequencies maintained its association with reward, while the other two frequencies were either switched to reward omission or punishment (**Figure 5A**). Operant “Go” responses (≥7 licks in 2.8s) were initially high to all tone frequencies following the abrupt change in reinforcement outcome (**Figure 5B**) but mice gradually reduced Go responses to the tone associated with a neutral outcome to approximately 40% of trials on average and reduced the Go response to the tone associated with tongue shock to approximately 25% of trials (**Figure 5C**).

This arrangement allowed us to contrast BFCN responses in HDB and GP/SI elicited by reward delivery, reward omission, and punishment (**Figure 5D**). We observed that BFCN responses to anticipated rewards were very weak in both HDB and GP/SI (**Figure 5E**). The omission of an anticipated reward was associated with a moderate response in HDB that was

significantly greater than both reward delivery response from the same fiber and the reward omission response in GP/SI. Delivery of silent, noxious stimulus elicited the strongest BFCN responses in both regions, although the response to shock was significantly greater in GP/SI than HDB (Figure 5E). BFCN response latencies to reward omission were significantly slower than other reinforcement types (mean ± SEM for omission vs. reward and shock; 1.04 ± 0.03 vs. 0.63 ± 0.03 seconds, for HDB and GP/SI, respectively; **Figure 5F**). The timing of the reward omission response was more precisely locked to lick bout offset than to timing of when reward would have been delivered. However, the response is not likely to movement per se, because activity levels following lick bout cessation were significantly greater on reward omission trials than on trials were the reward was delivered and consumed (**Figure 5 – figure supplement 1**). Recordings from unidentified basal forebrain neuron types in primates demonstrate that reward-omission responses only in a sub-type of neurons with slower, ramping responses (Zhang et al., 2019). Our observation of slower developing omission responses supports prior descriptions of reward timing and reinforcement prediction error encoding in BFCNs (Chubykin et al., 2013; Sturgill et al., 2020).

Learning-related enhancement of punishment-related auditory

Our earlier work used a Pavlovian learning paradigm to identify a transient, selective enhancement of GP/SI BFCN spike rates to the conditioned tone frequency that emerged within minutes of pairing sound with aversive air puffs and a slower, persistent enhancement of cue-evoked fiber-based GCaMP responses in GP/SI that emerged one day after the initial pairing of sounds with foot shock to “fill in” the silent gap separating the auditory cue and the delayed air puff (Guo et al., 2019). Here, we observed that BFCN responses to reward-predictive cues were not enhanced over the course of associative learning (Figure 3I). To reconcile these findings with our prior study, we examined whether auditory cues predicting aversive stimuli were enhanced as mice learned to change the reinforcement association from reward to punishment.

When compared with pre-reversal responses, cue-evoked responses in HDB remain relatively constant over the remainder of conditioning, showing no significant differences between reward-related, omission-related or punishment-related cues or over the course of training (**Figure 6A**). In GP/SI, cue-evoked responses for the tone frequency mapped to shock were enhanced within a few testing sessions following the reversal, while responses to the tone frequencies associated with reward and reward omission remained relatively stable (**Figure 6B**). We repeated the same analysis approach used for the all-appetitive phase of the task by discretizing behavioral sessions into five time bins based on the fraction of training completed. These data confirm that sound-evoked responses are greater overall in GP/SI than HDB but are not enhanced in either structure for cues associated with anticipated reward or the unanticipated omission of reward. The only exception was GP/SI, where cue-evoked responses increased by approximately 150% as the animal learned the new association between sound and punishment (**Figure 6C**).

Discussion

Progress towards understanding basal forebrain contributions to brain function and behavior has benefited from approaches that support recordings from genetically identified cholinergic and GABAergic cell types in behaving animals (Yang et al., 2017). Even when experiments are largely performed on a single species (mice) and focus largely on a single neurochemical cell type (cholinergic neurons), there have still been inconsistencies in the conclusions drawn from different experiments, particularly with respect to how BFCN activity relates to movement, to reward, to conditioned versus unconditioned sensory cues, and to predicting behavioral outcomes from cue-related activity. We reasoned that this variability could reflect differences in measurement technique, inter-subject variation, and differences in where the recordings were made along the extent of the rostrocaudal basal forebrain. To address this possibility, we developed an approach to study all of the experimental features listed above in each of our subjects while making simultaneous recordings from rostral and caudal regions of the cholinergic basal forebrain that are known to have distinct afferent and efferent connections.

The findings reported here can be summarized by identifying experimental features where HDB was more strongly involved than GP/SI, where GP/SI was more strongly involved than HDB, where both structures were equivalently recruited, and where neither structure showed strong involvement (**Figure 7**). HDB, perhaps on account of its strong reciprocal connectivity with the prefrontal cortex, showed a stronger involvement than GP/SI on variations of pupil-indexed internal brain state, in predicting whether the perceptual outcome in a behavioral detection task was a hit or a miss, and in encoding the omission of anticipated rewards (Gielow and Zaborszky, 2017; Rye et al., 1984; Zaborszky et al., 2012). Conversely, GP/SI, perhaps on account of stronger relative inputs from the striatum and thalamic regions encoding nociceptive inputs and auditory stimuli, showed a stronger functional selectivity for auditory stimuli, self-initiated movements, punishment, and learning-related plasticity of auditory cues associated with punishment (Chavez and Zaborszky, 2017; Rye et al., 1984; Zaborszky et al., 2012).

Specialized processing in the caudal tail of the cholinergic basal forebrain

Among these statistically significant regional differences, many were differences of degree, but a few were more akin to differences of kind. In particular, “native” BFCN responses to unconditioned auditory stimuli were markedly stronger in GP/SI compared with HDB, as was learning-related enhancement of punishment-predicting auditory cues. Other reports of BFCNs have either observed that cue-evoked responses only emerge after a learned association with reward (Crouse et al., 2020; Kuchibhotla et al., 2017; Parikh et al., 2007; Sturgill et al., 2020) or were not obviously present either for reward- or punishment-predicting cues (Hangya et al., 2015). Our interpretation is that native responses to unconditioned auditory cues would only be found in specific regions of the basal forebrain that receive bottom-up inputs from subcortical nuclei that encode auditory sound features. This includes the extreme caudal tail of the basal forebrain, GP/SI, where cholinergic neurons receive monosynaptic inputs from the auditory thalamus and tail of the striatum (Chavez and Zaborszky, 2017) and exhibit well-tuned short-latency (~10ms) spiking responses to moderate intensity tones and noise bursts (Chernyshev and Weinberger, 1998; Guo et al., 2019; Maho et al., 1995) as well as the medial septum,

where unidentified single units receive inputs from the pontine central gray and also exhibit short latency auditory responses outside of a learning context, though only to high-intensity broadband sounds (Zhang et al., 2017). Given that the GP/SI is the predominant source of BFCN input to lateral neocortical regions including ACtx, one interesting implication is that unconditioned auditory stimuli occurring outside of a behavioral context should elicit clear ACh transients in the downstream cortical targets of these neurons. Learning-related cortical plasticity requires transient neuromodulatory surges and does not occur when stimuli are presented in a passive context (Froemke, 2015), which underscores the central importance of mechanisms that not only coordinate properly timed basal forebrain cholinergic release, but also coordinate other permissive signatures for cortical plasticity and learning, such as BFCN-cortex synchrony (as characterized during auditory learning (Guo et al., 2019) and attentionally demanding auditory tasks (Laszlovszky et al., 2020)).

As for the learning-related enhancement of punishment-predicting - but not reward-predicting cues in GP/SI - this again may reflect the unique input this region of the basal forebrain receives from the medial geniculate and intralaminar thalamic groups, which also exhibit rapid, selective, and long-lasting enhanced spiking to tones associated with aversive stimuli (Edeline and Weinberger, 1992; Weinberger, 2011). Learned enhancement of reward-predicting auditory cues have been observed in more nucleus basalis BFCN axons innervating the basolateral amygdala (Crouse et al., 2020) and auditory cortex (Kuchibhotla et al., 2017), and have only been described in putative non-cholinergic neurons in HDB (Lin and Nicolelis, 2008), which therefore offers no point of contradiction with the absence of reward-related enhancement reported here in HDB and GP/SI BFCNs. Collectively, these findings point towards the caudal tail of the basal forebrain, which provides the strongest overall projection from the basal forebrain to ACtx and where approximately 80% of the neurons are cholinergic (Guo et al., 2019; Kamke et al., 2005; Rye et al., 1984), as a hub for encoding and associating sound with aversive, noxious stimuli, and for regulating inhibitory microcircuits within ACtx for long-term plasticity to enhance the representation of threat-predicting sounds (David et al., 2012; Guo et al., 2019; Letzkus et al., 2011).

Collectively, our findings support the view that the cholinergic basal forebrain broadcasts a largely homogeneous signal to its distributed downstream targets throughout the brain, yet regional afferent and efferent connectivity differences – particularly in the caudal tail of the basal forebrain – support regional specializations for regulating distinct features of global brain states, behavioral reinforcement, and perceptual salience. Interestingly, a neighboring region to GP/SI in the tail of the striatum also receive specialized dopaminergic inputs that do not encode reward value, but rather are activated by potentially threatening sensory stimuli (Menegas et al., 2018). This raises the interesting suggestion that cholinergic and dopaminergic signaling in the caudal tail of the striatum, GP, and SI may act differently than their classic actions elsewhere in the brain, by functioning as a hub for encoding threatening signals and selecting adaptive threat avoidance behaviors (Watabe-Uchida and Uchida, 2018)

Technical considerations in the interpretation of these findings

To address regional specializations within the cholinergic basal forebrain and minimize inter-subject variability across a wide range of sensory, motor, internal state, and task-related variables, we elected to use dual fiber-based chronic calcium imaging in Chat-Cre × GCaMP6f reporter mice. Using cre-expressing mice for functional characterizations of cholinergic neurons can be challenging. ChAT$_{(BAC)}$-Cre and ChAT$_{(IRES)}$-Cre homozygous mice exhibit behavioral irregularities that can be avoided by using ChAT$_{(IRES)}$-Cre hemizygous littermates (Chen et al., 2018). Ectopic expression in glia and non-cholinergic neurons can also be a problem, even in popular ChAT$_{(IRES)}$-Cre lines, either because the presence of a *frt*-flanked neo cassette can result in off-target expression, or because a fraction of glutamatergic neurons express ChAT transiently during development and would therefore still be labeled with cre-based transgenic expression approaches (Nasirova et al., 2020). Here, we used hemizygous offspring from the ChAT-CreΔneo line, in which the neo cassette is removed to reduce ectopic expression (Nasirova et al., 2020). Although we observed that expression was specific to ChAT+ neurons in the regions studied here (Figure 1C-D) and closely related to ACh3.0 fluorescence dynamics in a common downstream target (Figure 1H-J), we confirmed aberrant expression in brain regions outside of the basal forebrain, including both an absence of GCaMP expression in ChAT+ cells (e.g., in striatal interneurons) and ectopic expression of GCaMP in ChAT- cells (e.g., in neocortex and hippocampus). Therefore, while a transgenic reporter strategy was appropriate for our study to produce consistent and selective expression in two regions of the basal forebrain that were aligned to our fibers, due diligence is required before attempting selective cholinergic recordings from other brain regions.

Another caveat in the interpretation of fiber-based GCaMP imaging is that it provides a bulk signal that does not distinguish between somatic and neuropil-based calcium signals, nor between distinct types of BFCNs. That said, from a technical perspective, fiber-based imaging was clearly the best methodology to address our experimental aims. Efferent HDB axons leave the basal forebrain in a medial and dorsal orientation, coming nowhere near the GP/SI fiber, which ensures that each region could be measured independently (Bloem et al., 2014). Further, BFCNs in GP/SI are arrayed in a thin ventrodorsal sheet along the lateral wall of the internal capsule and then split into thin vertically oriented arrangements along the medial and lateral boundaries of the external GP (Clayton et al., 2020; Guo et al., 2019). This anatomy is not conducive to endoscopic imaging through implanted lenses, as the cells would not be visualized in a single focal plane and the large lens diameter would impact the internal capsule. Two-photon imaging of the cortical axon terminals from GP/SI BFCNs is feasible (Nelson and Mooney, 2016), though these signals would still arise from an indeterminate number of neurons and concerns about tissue bleaching and photodamage would not be compatible with the hours of daily testing over 30+ consecutive days that was performed here. Antidromic or somatic optogenetic tagging of single BFCNs is the gold standard, affording the highest level of spatial and temporal resolution. Our prior work used the antidromic variant of this approach to make targeted single unit recordings from GP/SI BFCNs that project to ACtx, but the yield was punishingly low (~1% of all units recorded) and units could not be held long enough to measure responses to each of the experimental variables tested here (Guo et al., 2019).

Cholinergic regulation of perceptual salience

Although the proportion of cholinergic neurons declines rostral to GP/SI, the overall spatial arrangement and larger cell body size of BFCNs in nucleus basalis and HDB makes somatic optogenetic tagging of single units somewhat more feasible (Hangya et al., 2015; Laszlovszky et al., 2020). An elegant recent study has demonstrated that BFCNs within nucleus basalis and HDB are not an indivisible class, but can themselves be further sub-divided into bursting and regular-firing BFCNs, where the proportion of each type varied across the rostral-caudal extent of the basal forebrain and had distinct patterns of synchronization both with respect to each other and with network oscillations measured in ACtx (Laszlovszky et al., 2020). Interestingly, when studied in the context of an auditory task similar to the paradigm used here, the spike timing of bursting BFCNs showed a stronger coupling with the ACtx on trials where mice made a Go response (regardless of whether it was a hit or false positive) whereas the regular-firing BFCNs showed a stronger coupling with the ACtx on trials where mice made the correct response (regardless of whether it was Go or NoGo).

Although fiber-based BFCN imaging cannot distinguish between the involvement of each cell type, we also noted a striking correspondence between GCaMP activity in the peri-tone period and the subsequent behavioral outcome (either hit or miss, Figure 3H-I). When measuring spiking of single BFCN units, a relationship to behavioral outcome was only observed in the period after the auditory cue was delivered, whereas we observed a clear connection to trial outcome after tone onset but also during the preceding 1s baseline period (thereby obviating any confound related to differences in licking activity between hit and miss trials). Prior studies have also reported that cholinergic levels prior to auditory onset can predict whether the animal would subsequently produce the correct or incorrect operant response, suggesting the bulk measures may be sensitive to pre-cue dynamics that are not resolvable at the level of single neurons (Kuchibhotla et al., 2017; Parikh et al., 2007). In a recent study, we found that hit or miss trial outcomes in a challenging auditory detection task could be predicted from the degree of synchrony in local networks of ACtx layer 2/3 pyramidal neurons measured from a 1s period prior to the delivery of the auditory cue (Resnik and Polley, 2021). As the cholinergic basal forebrain has classically been studied as a master regulator of cortical network synchrony (Buzsaki et al., 1988; Metherate et al., 1992), one clear suggestion is that ongoing cholinergic dynamics in the period preceding environmental sensory cues strongly regulate cortical network state, which can have profound impacts on the accurate encoding of sensory cues and appropriate selection of cue-directed actions.

Materials and Methods

Animals

All procedures were approved by the Massachusetts Eye and Ear Animal Care and Use Committee and followed the guidelines established by the National Institutes of Health for the care and use of laboratory animals. Male ChAT-cre-ΔNeo (homozygous, Jackson Labs

031661) and female AI148 mice (hemizygous, Jackson Labs 030328) were bred in house to generate mice of both sexes for this study. Offspring were therefore hemizygous for ChAT-cre-ΔNeo and either had hemizygous expression of cre-dependent GCaMP6f (ChAT+/GCaMP+) or did not express GCaMP (ChAT+/GCaMP-). Offspring genotypes were confirmed by PCR (Transnetyx probes) and by histology following perfusion.

Experiments were performed in adult mice, 2-3 months of age at the time the first measurement was performed. Prior to behavioral testing, mice were maintained on a 12 hr light/12 h dark cycle with ad libitum access to food and water. Mice were grouped-housed unless they had undergone a major survival surgery. Dual fiber imaging of ChAT neuron GCaMP fluorescence in GP/SI and HDB was performed in 11 ChAT+/GCaMP+ mice, four of which were used for additional histological quantification. Fiber imaging of ACh3.0 sensor fluorescence in ACtx was performed in 10 ChAT+/GCaMP- mice.

Surgical procedure for GCaMP photometry

Mice were anesthetized with isoflurane in oxygen (5% induction, 2% maintenance) and placed in a stereotaxic frame (Kopf Model 1900). A homeothermic blanket system was used to maintain body temperature at 36.6º (FHC). Lidocaine hydrochloride was administered subcutaneously to numb the scalp. The dorsal surface of the scalp was retracted and the periosteum was removed. Dual optic fiber implants (Doric, 400μm core 0.48NA, 1.25mm diameter low-autofluorescence metal ferrule) were slowly lowered into HDB (0.9 x 0.3 x 4.7) and GP/SI (2.5 x -1.5 x 3.3 mm from bregma, [lateral x caudal x ventral]) in the right hemisphere. Silicon adhesive (WPI Kwik-Sil) was applied to the exposed brain surface. The exposed skull surface was prepped with etchant (C&B metabond) and 70% ethanol before affixing a titanium head plate (iMaterialise) to the skull with dental cement (C&B Metabond). At the conclusion of the procedure, Buprenex (0.05 mg/kg) and meloxicam (0.1 mg/kg) were administered and the animal was transferred to a warmed recovery chamber.

Surgical procedure for Acetylcholine Sensor Photometry

The initial surgical procedures and perioperative care were similar to that for GCaMP photometry. The skull overlying the right ACtx exposed by moving the temporalis muscle. A burr hole was made on the temporal ridge at 2.9mm posterior to bregma, using a 31-gauge needle. A motorized injection system (Stoelting) was used to inject 200nL of AAV9-hSyn-ACh3.0 (diluted 10% in sterile saline from 3.45 x 10^{13} genome copies/mL) via a pulled glass micropipette 0.5mm below the pial surface. We waited at least 10 minutes following the injection prior to withdrawing the micropipette. A tapered fiber (Optogenix, NA 0.39, diameter 200 μm, active length 1.0 mm) was implanted 1mm below the pial surface and secured using dental cement dyed with India Ink, which also secured the titanium head plate. Sensor photometry experiments began three weeks following the injection.

Pupillometry

Mice were habituated to head-fixation during three sessions of 15, 30, and 60 minutes. Video recordings of the pupil under iso-luminous background conditions were performed during the final habituation session and the following sensory characterization day. Video recordings were made at 30Hz with a CMOS camera (Teledyne Dalsa, model M2020) outfitted with a lens (Tamron 032938) and infrared longpass filter (Midopt lp830-25.5). Automated analysis of pupil diameter follows the procedure described previously by McGinley and colleagues (McGinley et al., 2015b). Briefly, each movie was thresholded such that most pixel values within the pupil were below threshold and all other pixels were above threshold. A circle was fit to the pupil by first calculating the center of mass within the pupil and then centering a circle with the corresponding area to that point. Canny edge detection was then used to identify edge pixels within each grayscale image. Edge pixels were removed if they were more than 3 pixels away from a pupil pixel or outside of an annulus with diameters that were 0.5 and 1.75 the diameter of the initial fit circle. As a final step, an ellipse was fit to the remaining edge pixels using least-squares regression and the pupil diameter was defined from the diameter of a circle with a matching area. This procedure was performed for each image frame using a Matlab (Mathworks) script adapted from the original publication (McGinley et al., 2015b).

Pupil diameter for ACh3.0 sensor imaging experiments was extracted using DeepLabCut (version 2.1.8.2, (Nath et al., 2019). Specifically, three investigators each labeled 100 frames taken from 10 mice, for a total of 300 frames from 30 mice. The four cardinal and four intercardinal compass points were marked for each pupil. Marker placement was confirmed by at least one additional investigator. 95% of frames were used for training. We used a ResNet-101 based neural network with default parameters for 1,030,000 training iterations. We then used a p-value cutoff of 0.9 to condition the X,Y coordinates for analysis. This network was then used to analyze videos from similar experimental settings from the ten ACh3.0 sensor imaging mice. We calculated pupil diameter for each frame by fitting an ellipse to the identified pupil contour points using a least-squares criterion and calculating the long axis diameter.

Operant behavioral testing

All mice proceeded through the same series of tests beginning two weeks following fiber implant surgery (Figure 2A). On days 1 and 2, mice were habituated to head fixation within the behavioral test chamber. On day 3, pupillometry was performed without sensory stimulation. On day 4, pupillometry and fiber imaging was performed in response to the presentation of auditory or visual stimuli. Beginning on day 5, mice were placed on water restriction and were monitored until they reached 80% of their baseline weight. Beginning on day 8 or 9, mice began appetitive operant training that rewarded vigorous licking shortly following the presentation of three different tone frequencies. Finally, on day 13-22, mice were switched to a reinforcement reversal task, where two of the previously rewarded frequencies were switched to neutral or aversive reinforcement. These methods for each of these stages are provided in detail below.

Sensory characterization:

Visual gratings were generated in Matlab using the Psychtoolbox extension and presented via an 800 x 480 pixel display (Adafruit 2406) positioned approximately 15cm from the left eye 45 degrees of midline. Visual gratings were presented with a spatial frequency of 0.035 cycles per degree at three contrasts: 11%, 33%, and 100%. Gratings (2s duration) were presented at both vertical and horizontal orientations. Spatial drift (2Hz) was imposed along the orthogonal axis to orientation.

Auditory stimuli were either pure tones or auditory drifting gratings (i.e., ripples). Stimuli were generated with a 24-bit digital-to-analog converter (National Instruments model PXI-4461) and presented via a free-field speaker (CUI, CMS0201KLX) placed approximately 10 cm from the left (contralateral) ear canal. Free-field stimuli were calibrated using a wide-band free-field microphone (PCB Electronics, 378C01). Pure tones were low (either 6 or 6.8 kHz), mid (9.5 or 11.3 kHz), or high (13.9 or 18.5 kHz) frequencies presented at 3 intensities (30, 50, and 70 dB SPL). Tones were 0.4s duration shaped with 5ms raised cosine onset and offset ramps. Auditory gratings ranged from 2-45kHz with 2s duration (5ms raised cosine onset and offset ramps), presented at downward and upward frequency trajectories (at -2 and +2 Hz) at three intensities (30, 50, and 70 dB SPL). The spectrum was shaped with 20 frequency carriers per octave that were sinusoidally modulated with 90% depth at 1 cycle per octave.

A single block consisted of 22 unique stimulus trials with a 7s inter-trial interval (6 visual gratings [2 orientations x 3 contrasts], 9 tones [3 frequencies x 3 levels], 6 auditory gratings [2 directions x 3 intensities] and 1 “nothing” trial where neither an auditory nor visual stimulus was presented). The stimulus order was randomly determined for each of 20 presentation blocks.

Operant training:

Behavioral shaping for the rewarded tone detection task began immediately following the sensory characterization session. In the initial phase of training, mice learned to vigorously lick a spout shortly following tone onset (low-, mid-, or high-frequency, as specified above at 70 dB SPL) in order receive a liquid reward (10% sucrose in water, 1.5 μL per reward, 1 reward per trial). Initially, tones were paired with rewards (i.e., Pavlovian conditioning), initiated 0.5s after tone onset.

Once mice were reliably licking prior to reward onset, the lick requirement to trigger reward delivery (i.e., operant conditioning) was progressively increased. The licking criterion to receive a reward was 7 lickspout contacts within a 2.8s period beginning 0.2s after stimulus onset, where the interval between any two consecutive licks could not exceed 1s. Individual trials were scored as hits, according to the criterion above, misses (no licks), or partial hits (lickspout contact that did not meet the criterion above). Intertrial intervals were determined randomly from a truncated exponential distribution within a range of 7-10s. Trials were aborted in the event of lick spout contact in a withhold period of 2s (initial phase) or 1.5s (after reversal) preceding stimulus onset. Generally, mice learned to produce 7 licks in 2.8s to initiate reward with low false alarm rates within 2-3 sessions.

In order to analyze licking-related activity, separate lick bouts were also selected from the inter-trial periods without stimuli or reward. Lick bouts were defined as at least two lick contacts less than 250ms apart, bookended by quiescent lick-free periods at least 1s each before and after the bout.

Once the reward rate exceeded 70% across all frequencies for at least one session, mice were transitioned to the reversal stage of the operant task in which one of the three tones remained associated with reward, one was associated with shock, and a third was not associated with reward or punishment (i.e., neutral outcome). The assignment of tone frequency to reinforcement condition was randomized across mice. Punishment was delivered by briefly electrifying the lick spout (0.6mA for 0.4s) once the lick bout threshold (7 licks in 2.8s) had been crossed. During this stage, the rewarded tone was presented on 50% of trials and the rewarded and neutral tones were each presented on 25% of trials. Operant testing was terminated once the Go probability stabilized across all tone frequencies for at least two consecutive days.

Fiber photometry

Data acquisition:

LEDs of different wavelengths provided a basis for separating calcium-dependent (465 nm) and calcium-independent (405nm) fluorescence. Blue and purple LEDs were modulated at 210Hz and 330Hz, respectively, and combined through an integrated fluorescence mini-cube (FMC4, Doric). The power at the tip of the patch cable was 0.1 - 0.2mW. The optical patch cable was connected to the fiber implant via a zirconia mating sleeve. Bulk fluorescent signals were acquired with a femtowatt photoreceiver (2151, Newport) and digital signal processor (Tucker-Davis Technologies RZ5D). The signal was demodulated by the lock-in amplifier implemented in the processor, sampled at 1017Hz and low-pass filtered with a corner frequency at 20Hz. The optical fiber were prebleached overnight by setting both LEDs to constant illumination at a low power (<50uW).

Data processing: After demodulation, the 465nm GCaMP responses were calculated as the fractional change in fluorescence DF/F_0, where F_0 was defined as the running median fluorescence value in a 60s time window. DF/F_0 traces were then low-pass filtered with a 2^{nd} order zero-lag Butterworth filter, with a cut-off frequency set to 7Hz. Event-related DF/F0 values were then z-scored relative to baseline activity levels. For passive sensory characterization experiments, the baseline distribution consisted of all DF/F_0 recorded during a 2s window preceding visual or auditory stimulus onset. For recordings made during the operant task, the baseline distribution consisted of all DF/F_0 recorded during a 2s period prior to auditory cue onset that was combined across trial types and sessions.

Data analysis: To measure the relationship with spontaneous pupil fluctuations (Figure 1), photometry data were first downsampled to 30Hz before measuring coherence with a hamming window of 1500 samples and 1400 sample overlap. Lag was defined by the peak of the cross-correlation between fluorescence (GCaMP or ACh3.0) and pupil fluctuations. Event-related response amplitudes (Figures 2-6) were calculated on an individual trial basis. To

measure sensory responses (Figure 2), the mean activity during a 2s baseline period immediately preceding stimulus onset was subtracted from the peak activity occurring within 2s following stimulus onset. Responses were averaged over upward and downward auditory ripples and over vertical and horizontal visual gratings. The amplitude of spontaneous transients (Figure 2D) were calculated on "nothing trials" (visual blank and auditory silent). A threshold was applied to DF/F_0 values for each trial to identify time points corresponding to the bottom 5% of fractional change values. Spontaneous transients were operationally defined as any time point containing a value that was at least 0.5 z-scores above the 5% threshold. Spontaneous activity was then quantified as the mean value for all suprathreshold values within the trial. Time windows used to calculate the various event-related response amplitudes related to the behavioral task (Figures 3-6) are defined in the corresponding figure legends.

Histology

At the conclusion of imaging, mice were deeply anesthetized and prepared for transcardial perfusion with a 4% formalin solution in 0.1M phosphate buffer. The brains were extracted and post-fixed at room temperature for an additional 12 hours before transfer to 30% sucrose solution. In a subset of brains (N=4), coronal sections (30um) were rinsed for 1 hour in 0.1M phosphate buffered saline (PBS) and 0.4% Triton-X, and then permeabilized for 1 hour with 1% Triton-X and 5% normal horse serum. Sections where incubated overnight in blocking solution containing the primary antibodies (Goat anti-ChAT 1:100, Millipore, AB144P). Sections were rinsed in PBS then incubated for 2 hours at room temperature in blocking solution containing secondary antibodies, counterstained in DAPI for 5 minutes, rinsed in PBS, mounted onto glass slides, and then coverslipped. Co-localization of ChAT and GCaMP was quantified in the HDB and GP/SI regions of interest immediately beneath the tip of the fiber path and in the corresponding region in the contralateral hemisphere. Regions of interest were imaged at 63x using a Leica DM5500B fluorescent microscope. Tiled image stacks were then separated into individual fluorophore channels and labeled cells were manually counted in each channel independently using Adobe Photoshop.

Statistics

All statistical analyses were performed in MATLAB 2016b (Mathworks). Data are reported as mean ± SEM unless otherwise indicated. Inflated familywise error rates from multiple comparisons of the same sample were adjusted with the Holm-Bonferroni correction. Statistical significance was defined as $p < 0.05$.

Acknowledgements

These studies were supported by NIH grant DC009836 (DP), The Nancy Lurie Marks Family Foundation (DP), a Herchel Smith Harvard Scholarship (BR), a Fondation Zdenek et Michaela Bakala Scholarship (BR), and NIH grant K08MH116135 (EK).

673 BR collected and analyzed the combined calcium imaging, pupillometry and behavioral data.
674 EK, YW, and TC collected and analyzed the combined ACh3.0 sensor and pupillometry data.
675 MJ and YL developed the ACh3.0 sensor purchased for use in these experiments. BR and DP
676 designed the experiments. DP and BR prepared the figures. DP wrote the manuscript, with
677 input from all authors.
678
679 We thank Ken Hancock for programming additional changes in his behavioral neurophysiology
680 data collection software. We thank Matt McGinley for hardware advice and software support
681 for pupil diameter quantification. We thank Troy Hackett for support developing our
682 immunolabeling and histology quantification protocols.
683
684
685 **Competing interests**
686 The authors declare that no competing interests exist.
687
688
689
690
691
692
693
694
695
696
697
698
699
700
701
702
703
704
705
706
707
708
709
710
711
712
713
714
715

References

Becket Ebitz, R., and Moore, T. (2019). Both a gauge and a filter: Cognitive modulations of pupil size. Front. Neurol. *10*, 1–14.

Bloem, B., Schoppink, L., Rotaru, D.C., Faiz, A., Hendriks, P., Mansvelder, H.D., van de Berg, W.D.J., and Wouterlood, F.G. (2014). Topographic mapping between basal forebrain cholinergic neurons and the medial prefrontal cortex in mice. J. Neurosci. *34*, 16234–16246.

Buzsaki, G., Bickford, R.G., Ponomareff, G., Thal, L.J., Mandel, R., and Gage, F.H. (1988). Nucleus basalis and thalamic control of neocortical activity in the freely moving rat. J. Neurosci. *8*, 4007–4026.

Chavez, C., and Zaborszky, L. (2017). Basal forebrain cholinergic-auditory cortical network: primary versus nonprimary auditory cortical areas. Cereb. Cortex *27*, 2335–2347.

Chen, E., Lallai, V., Sherafat, Y., Grimes, N.P., Pushkin, A.N., Fowler, J.P., and Fowler, C.D. (2018). Altered baseline and nicotine-mediated behavioral and cholinergic profiles in ChAT-Cre mouse lines. J. Neurosci. *38*, 2177–2188.

Chernyshev, B. V., and Weinberger, N.M. (1998). Acoustic frequency tuning of neurons in the basal forebrain of the waking guinea pig. Brain Res. *793*, 79–94.

Chubykin, A.A., Roach, E.B., Bear, M.F., and Shuler, M.G.H. (2013). A cholinergic mechanism for reward timing within primary visual cortex. Neuron *77*, 723–735.

Clayton, K.K., Williamson, R.S., Hancock, K.E., Tasaka, G., Mizrahi, A., Hackett, T.A., and Polley, D.B. (2020). Auditory corticothalamic neurons Are recruited by motor preparatory inputs. Curr. Biol. *31*, 1–13.

Crouse, R.B., Kim, K., Batchelor, H.M., Girardi, E.M., Kamaletdinova, R., Chan, J., Rajebhosale, P., Pittenger, S.T., Role, L.W., Talmage, D.A., et al. (2020). Acetylcholine is released in the basolateral amygdala in response to predictors of reward and enhances the learning of cue-reward contingency. ELife *9*, 1–31.

David, S. V, Fritz, J.B., and Shamma, S.A. (2012). Task reward structure shapes rapid receptive field plasticity in auditory cortex. Proc. Natl. Acad. Sci. *109*, 2144–2149.

Disney, A.A., and Higley, M.J. (2020). Diverse spatiotemporal scales of cholinergic signaling in the neocortex. J. Neurosci. *40*, 720–725.

Do, J.P., Xu, M., Lee, S.H., Chang, W.C., Zhang, S., Chung, S., Yung, T.J., Fan, J.L., Miyamichi, K., Luo, L., et al. (2016). Cell type-specific long-range connections of basal forebrain circuit. ELife *5*, 1–18.

Edeline, J.M., and Weinberger, N.M. (1992). Associative retuning in the thalamic source of input to the amygdala and auditory cortex: receptive field plasticity in the medial division of the medial geniculate body. Behav. Neurosci. *106*, 81–105.

Everitt, B.J., and Robbins, T.W. (1997). Central cholinergic systems and cognition. Annu. Rev. Psychol. *48*, 649–684.

Froemke, R.C. (2015). Plasticity of cortical excitatory-inhibitory balance. Annu. Rev. Neurosci. *38*, 195–219.

Gielow, M.R., and Zaborszky, L. (2017). The Input-Output Relationship of the Cholinergic Basal Forebrain. Cell Rep. *18*, 1817–1830.

Gritti, I., Henny, P., Galloni, F., Mainville, L., Mariotti, M., and Jones, B.E. (2006). Stereological

estimates of the basal forebrain cell population in the rat, including neurons containing choline acetyltransferase, glutamic acid decarboxylase or phosphate-activated glutaminase and colocalizing vesicular glutamate transporters. Neuroscience *143*, 1051–1064.

Guo, W., Robert, B., and Polley, D.B. (2019). The cholinergic basal forebrain links auditory stimuli with delayed reinforcement to support learning. Neuron *103*.

Hangya, B., Ranade, S.P., Lorenc, M., and Kepecs, A. (2015). Central cholinergic neurons are rapidly recruited by reinforcement feedback. Cell *162*, 1155–1168.

Harrison, T.C., Pinto, L., Brock, J.R., and Dan, Y. (2016). Calcium imaging of basal forebrain activity during innate and learned behaviors. Front. Neural Circuits *10*, 1–12.

Jing, M., Li, Y., Zeng, J., Huang, P., Skirzewski, M., Kljakic, O., Peng, W., Qian, T., Tan, K., Zou, J., et al. (2020). An optimized acetylcholine sensor for monitoring in vivo cholinergic activity. Nat. Methods *17*, 1139–1146.

Kamke, M.R., Brown, M., and Irvine, D.R.F. (2005). Origin and immunolesioning of cholinergic basal forebrain innervation of cat primary auditory cortex. Hear. Res. *206*, 89–106.

Kim, T., Thankachan, S., McKenna, J.T., McNally, J.M., Yang, C., Choi, J.H., Chen, L., Kocsis, B., Deisseroth, K., Strecker, R.E., et al. (2015). Cortically projecting basal forebrain parvalbumin neurons regulate cortical gamma band oscillations. Proc. Natl. Acad. Sci. *112*, 201413625.

Kuchibhotla, K. V, Gill, J. V, Lindsay, G.W., Papadoyannis, E.S., Field, R.E., Sten, T.A.H., Miller, K.D., and Froemke, R.C. (2017). Parallel processing by cortical inhibition enables context-dependent behavior. Nat. Neurosci. *20*, 62–71.

Laszlovszky, T., Schlingloff, D., Hegedüs, P., Freund, T.F., Gulyás, A., Kepecs, A., and Hangya, B. (2020). Distinct synchronization, cortical coupling and behavioral function of two basal forebrain cholinergic neuron types. Nat. Neurosci. *23*, 992–1003.

Letzkus, J.J., Wolff, S.B.E., Meyer, E.M.M., Tovote, P., Courtin, J., Herry, C., and Lüthi, A. (2011). A disinhibitory microcircuit for associative fear learning in the auditory cortex. Nature *480*, 331–335.

Li, X., Yu, B., Sun, Q., Zhang, Y., Ren, M., Zhang, X., Li, A., Yuan, J., Madisen, L., Luo, Q., et al. (2018). Generation of a whole-brain atlas for the cholinergic system and mesoscopic projectome analysis of basal forebrain cholinergic neurons. Proc. Natl. Acad. Sci. U. S. A. *115*, 415–420.

Lin, S.-C.C., and Nicolelis, M.A.L. (2008). Neuronal ensemble bursting in the basal forebrain encodes salience irrespective of valence. Neuron *59*, 138–149.

Lohani, S., Moberly, A.H., Benisty, H., Landa, B., Jing, M., Li, Y., Higley, M.J., and Cardin, J.A. (2020). Dual color mesoscopic imaging reveals spatiotemporally heterogeneous coordination of cholinergic and neocortical activity. BioRxiv 2020.12.09.418632.

Maho, C., Hars, B., Edeline, J.M., and Hennevin, E. (1995). Conditioned changes in the basal forebrain: Relations with learning-induced cortical plasticity. Psychobiology *23*, 10–25.

McGinley, M.J., Vinck, M., Reimer, J., Batista-Brito, R., Zagha, E., Cadwell, C.R., Tolias, A.S., Cardin, J.A., and McCormick, D.A. (2015a). Waking state: rapid variations modulate neural and behavioral responses. Neuron *87*, 1143–1161.

McGinley, M.J., David, S. V., and McCormick, D.A. (2015b). Cortical membrane potential signature of optimal states for sensory signal detection. Neuron *87*, 179–192.

Menegas, W., Akiti, K., Amo, R., Uchida, N., and Watabe-Uchida, M. (2018). Dopamine neurons projecting to the posterior striatum reinforce avoidance of threatening stimuli. Nat. Neurosci. *21*, 1421–1430.

Metherate, R., Cox, C.L., and Ashe, J.H. (1992). Cellular bases of neocortical activation: Modulation of neural oscillations by the nucleus basalis and endogenous acetylcholine. J. Neurosci. *12*, 4701–4711.

Monosov, I.E. (2020). How outcome uncertainty mediates attention, learning, and decision-making. Trends Neurosci. *43*, 795–809.

Nasirova, N., Quina, L.A., Agosto-Marlin, I.M., Ramirez, J.M., Lambe, E.K., and Turner, E.E. (2020). Dual recombinase fate mapping reveals a transient cholinergic phenotype in multiple populations of developing glutamatergic neurons. J. Comp. Neurol. *528*, 283–307.

Nath, T., Mathis, A., Chen, A.C., Patel, A., Bethge, M., and Mathis, M.W. (2019). Using DeepLabCut for 3D markerless pose estimation across species and behaviors. Nat. Protoc. *14*, 2152–2176.

Nelson, A., and Mooney, R. (2016). The basal rorebrain and motor cortex provide convergent yet distinct movement-related inputs to the auditory cortex. Neuron *90*, 635–648.

Parikh, V., Kozak, R., Martinez, V., and Sarter, M. (2007). Prefrontal acetylcholine release controls cue detection on multiple timescales. Neuron *56*, 141–154.

Pisano, F., Pisanello, M., Lee, S.J., Lee, J., Maglie, E., Balena, A., Sileo, L., Spagnolo, B., Bianco, M., Hyun, M., et al. (2019). Depth-resolved fiber photometry with a single tapered optical fiber implant. Nat. Methods *16*, 1185–1192.

Reimer, J., McGinley, M.J., Liu, Y., Rodenkirch, C., Wang, Q., McCormick, D.A., and Tolias, A.S. (2016). Pupil fluctuations track rapid changes in adrenergic and cholinergic activity in cortex. Nat. Commun. *7*, 13289.

Resnik, J., and Polley, D.B. (2021). Cochlear neural degeneration disrupts hearing in background noise by increasing auditory cortex internal noise. Neuron 1–13.

Rye, D.B., Wainer, B.H., Mesulam, M.M., Mufson, E.J., and Saper, C.B. (1984). Cortical projections arising from the basal forebrain: A study of cholinergic and noncholinergic components employing combined retrograde tracing and immunohistochemical localization of choline acetyltransferase. Neuroscience *13*, 627–643.

Sarter, M., and Lustig, C. (2020). Forebrain cholinergic signaling: Wired and phasic, not tonic, and causing behavior. J. Neurosci. *40*, 712–719.

Sturgill, J.F., Hegedus, P., Li, S.J., Chevy, Q., Siebels, A., Jing, M., Li, Y., Hangya, B., and Kepecs, A. (2020). Basal forebrain-derived acetylcholine encodes valence-free reinforcement prediction error. BioRxiv.

Teles-Grilo Ruivo, L.M., Baker, K.L., Conway, M.W., Kinsley, P.J., Gilmour, G., Phillips, K.G., Isaac, J.T.R., Lowry, J.P., and Mellor, J.R. (2017). Coordinated acetylcholine release in prefrontal cortex and hippocampus Is associated with arousal and reward on distinct timescales. Cell Rep. *18*, 905–917.

Watabe-Uchida, M., and Uchida, N. (2018). Multiple dopamine systems: Weal and woe of dopamine. Cold Spring Harb. Symp. Quant. Biol. *83*, 83–95.

Weinberger, N.M. (2011). The medial geniculate, not the amygdala, as the root of auditory fear conditioning. Hear. Res. *274*, 61–74.

Yang, C., Thankachan, S., McCarley, R.W., and Brown, R.E. (2017). The menagerie of the basal forebrain: how many (neural) species are there, what do they look like, how do they behave and who talks to whom? Curr. Opin. Neurobiol. *44*, 159–166.

Zaborszky, L., van den Pol, A., and Gyengesi, E. (2012). The basal forebrain cholinergic projection system in mice. In The Mouse Nervous System, C. Watson, G. Paxinos, and L. Puelles, eds. pp. 684–718.

Zekveld, A.A., Koelewijn, T., and Kramer, S.E. (2018). The pupil dilation response to auditory stimuli: current state of knowledge. Trends Hear. *22*, 1–25.

Zhang, G., Sun, W., Zingg, B., Shen, L., He, J., Xiong, Y., Tao, H.W., and Zhang, L.I. (2017). A non-canonical reticular-limbic central auditory pathway via medial septum contributes to fear conditioning. Neuron *97*, 406-417.e4.

Zhang, K., Chen, C.D., and Monosov, I.E. (2019). Novelty, salience, and surprise timing are signaled by neurons in the basal forebrain. Curr. Biol. *29*, 134-142.e3.

886 # Figures and Figure Legends

887

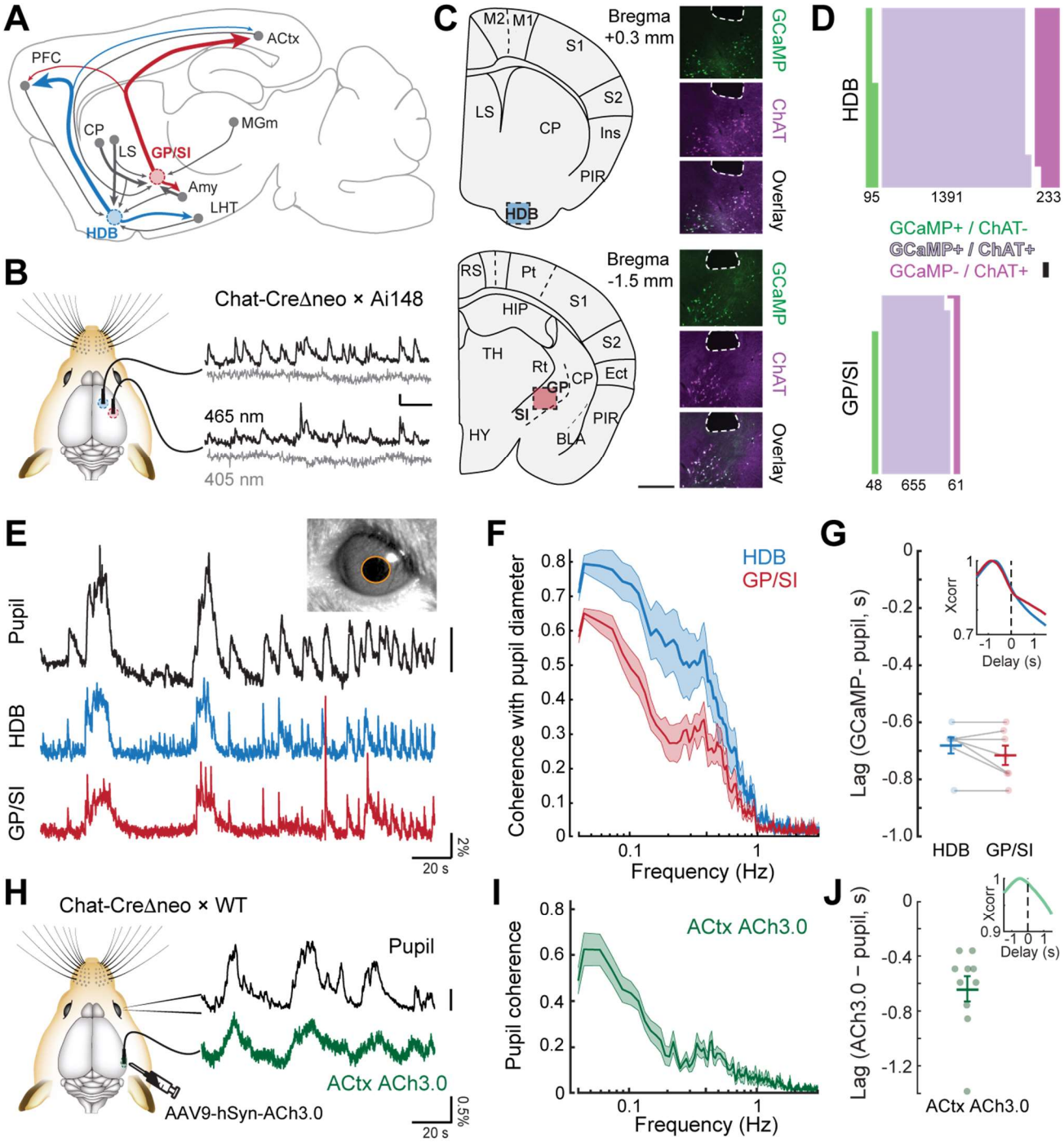

888

889

890 **Figure 1. Strong, but differential, coherence between pupil-indexed brain state and**
891 **cholinergic neural activity.**

892 (**A**) Mid-sagittal diagram of the mouse brain depicting the diversity in major inputs (gray) and
893 outputs (colored) between a rostroventral basal forebrain structure, the horizontal limb of the
894 diagonal band (HDB), and the caudodorsal tail of the basal forebrain, the boundary of the
895 globus pallidus and substantia innominata (GP/SI). ACtx = auditory cortex, MGm = medial

subdivision of the medial geniculate body, LHT = lateral hypothalamus, Amy = amygdala, LS = lateral septum, CP = caudate putamen, PFC = prefrontal cortex.

(**B**) Dual bulk fiber-based calcium imaging from basal forebrain cholinergic neurons was performed from the HDB and GP/SI of ChAT-Cre-Δneo × Ai148 mice. Dual wavelength imaging allowed separate visualization of calcium-independent fluorescence (405 nm) from calcium-dependent fluorescence (465 nm). Vertical and horizontal scale bars reflect 1% DF/F and 5 seconds, respectively.

(**C**) Coronal diagrams illustrate anatomical landmarks at the rostral (top) and caudal (bottom) imaging locations. Post-mortem fluorescence photomicrographs of brain sections immunolabeled for the ChAT protein depict the outline of the fiber path and the position of HDB, GP, and SI. GCaMP and ChAT fluorescence channels and their overlay to illustrate the strong co-localization of GCaMP in ChAT neurons within HDB and GP/SI regions near the fiber tip. Scale bar = 0.5mm.

(**D**) Cells near the fiber tip were counted based on their expression of GCaMP-only (green), ChAT-only (magenta), or both GCaMP and ChAT (violet). Numbers indicate the number of neurons in the corresponding category. Scale bar = 5 neurons.

(**E**) Isoluminous spontaneous pupil dilations in an example mouse were visualized in combination with GCaMP imaging from HDB and GP/SI. Pupil scale bar depicts a 5 pixel^2 areal change.

(**F**) Mean ± SEM coherence of HDB and GP/SI GCaMP activity with pupil-indexed brain state in isoluminous conditions without any explicit environmental stimuli or task demands. N = 7 mice provided data for pupil, HDB, and GP/SI. Basal forebrain GCaMP signals closely track slow (< 0.5Hz) changes in pupil diameter, though the correspondence is stronger overall in HDB than in GP/SI (2-way repeated measures ANOVA, main effect for brain structure, $F = 12.58$, $p = 0.01$).

(**G**) HDB and GP/SI GCaMP changes lead pupil fluctuations by approximately 0.7s. *Inset:* Cross-correlation of the HDB and GP/SI GCaMP signals with pupil fluctuations. Individual data points depict the time value corresponding to the peak of the cross-correlograms from individual mice. Mean ± SEM values are provided at left and right.

(**H**) Tapered fiber imaging of the ACh3.0 fluorescence during pupil videography. Scale bar depicts a 5 pixel diameter change.

(**I**) Mean ± SEM coherence of ACtx ACh3.0 with pupil-indexed arousal in isoluminous conditionswithout any explicit environmental stimuli or task demands. N = 10 mice. Pupil coherence looks qualitatively similar to GP/SI GCaMP coherence, which is expected on account of its stronger anatomical projection to ACtx.

(**J**) ACtx ACh3.0 changes lead pupil fluctuations by approximately 0.6s. *Inset:* Cross-correlation of the ACtx ACh3.0 signal with pupil fluctuations. Individual data points depict the time value corresponding to the peak of the cross-correlograms from individual mice. Mean ± SEM values are provided at left and right.

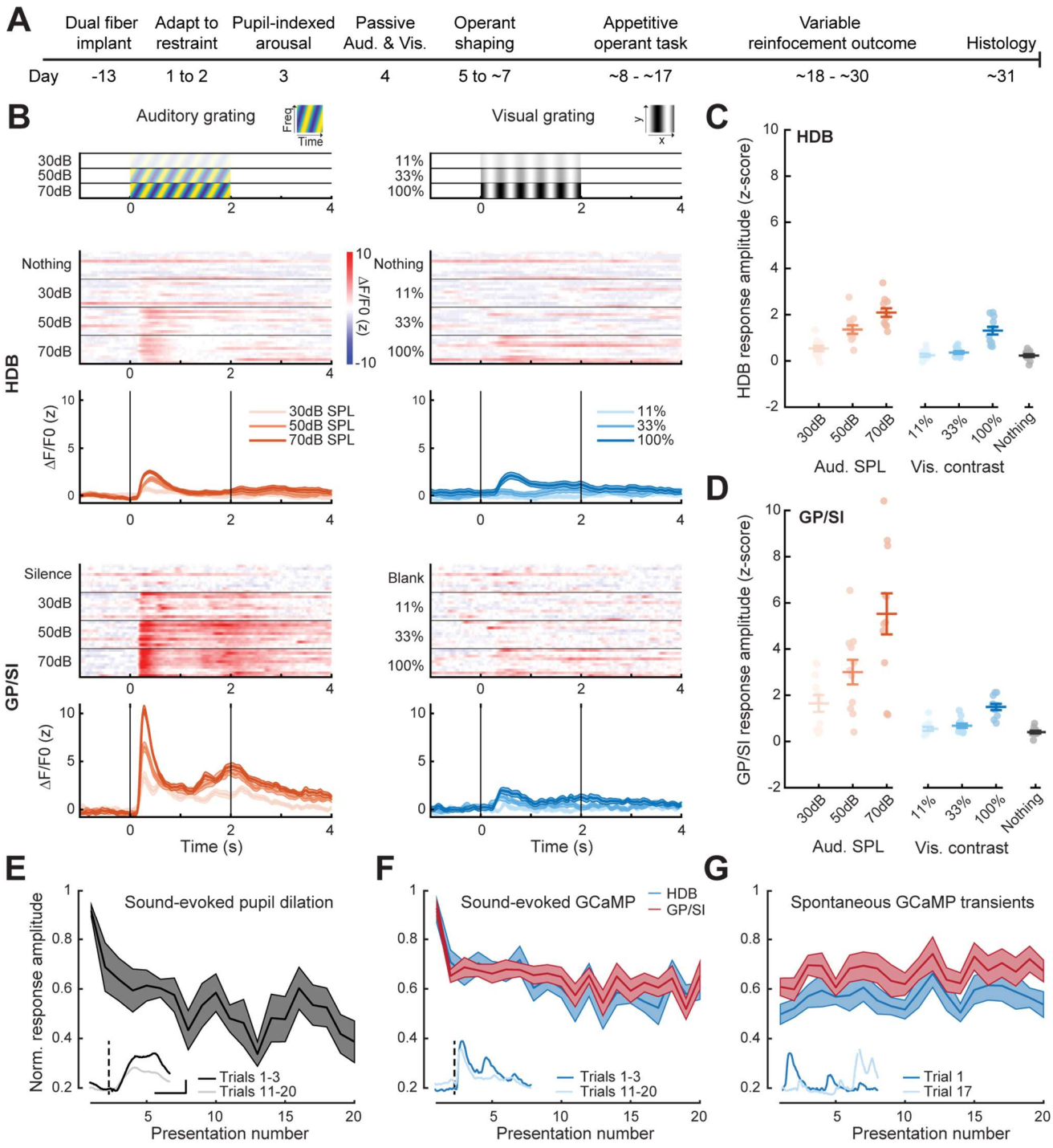

Figure 2. Strong, rapidly adapting to responses to auditory, but not visual, stimulation in GP/SI cholinergic neurons.

(**A**) Timeline for measurements and procedures performed in each of 11 ChAT-Cre-Δneo × Ai148 mice.

(**B**) Sensory-evoked responses to spectrotemporally modulated broadband sounds (i.e., ripples) of varying intensity and drifting visual gratings of varying contrast in an awake, passively listening example mouse. Heat maps depict fractional change values for individual

trials in HDB (left column) and GP/SI (right column). Line plots depict mean ± SEM z-scored fractional change across all trials. Vertical bars denote stimulus onset and offset.

(C-D) Z-scored response amplitudes to auditory and visual stimuli in HDB (*B*) and GP/SI (*C*). Circles denote individual mice (N=11 for all conditions), bars denote sample mean and SEM. "Nothing" denotes the mean response to silence and blank visual stimuli, which are excluded from the statistical analysis below. Sensory-evoked cholinergic responses increase with intensity and contrast, but are stronger overall in GP/SI, particularly in the auditory modality (3-way repeated measures ANOVA with structure, stimulus level, and modality as independent variables: Main effect for structure, $F = 18.74$, $p = 0.001$; Main effect for stimulus level, $F = 55.08$, $p = 7 \times 10^{-9}$; Main effect for modality, $F = 17.95$, $p = 0.002$; Modality × structure × level interaction term, $F = 10.25$, $p = 0.0009$).

(**E**) Mean ± SEM normalized pupil dilations evoked by 70 dB SPL auditory gratings significantly decreased over 20 presentations (One-way repeated measures ANOVA, $F = 2.85$, $p = 0.0003$; N = 7 mice). *Inset*: Mean sound-evoked pupil diameter change in an example mouse for trials 1-3 versus 11-20. Inset scale bar = 1 z-score and 2s and applies to all inset panels below. Vertical dashed line = onset of the 2s stimulus.

(**F**) Mean ± SEM normalized BFCN response to auditory gratings were significantly and equivalently reduced in HDB and GP/SI over 20 presentations (2-way repeated measures ANOVA with structure and presentation number as independent variables: Main effect for structure, $F = 0.51$, $p = 0.49$; Main effect for presentation number, $F = 6.11$, $p = 5 \times 10^{-12}$; N = 11 mice). *Insets*: Mean response from an HDB fiber of an example mouse for trials 1-3 versus 11-20.

(**G**) Mean ± SEM normalized BFCN spontaneous GCaMP transient amplitudes did not change over 20 measurement blocks (2-way repeated measures ANOVA with structure and presentation number as independent variables: Main effect for structure, $F = 0.80$, $p = 0.70$; Presentation number × structure interaction term, $F = 0.57$, $p = 0.93$; N = 11 mice). *Insets*: Spontaneous transients from an HDB fiber in two trials for which no stimulus was presented.

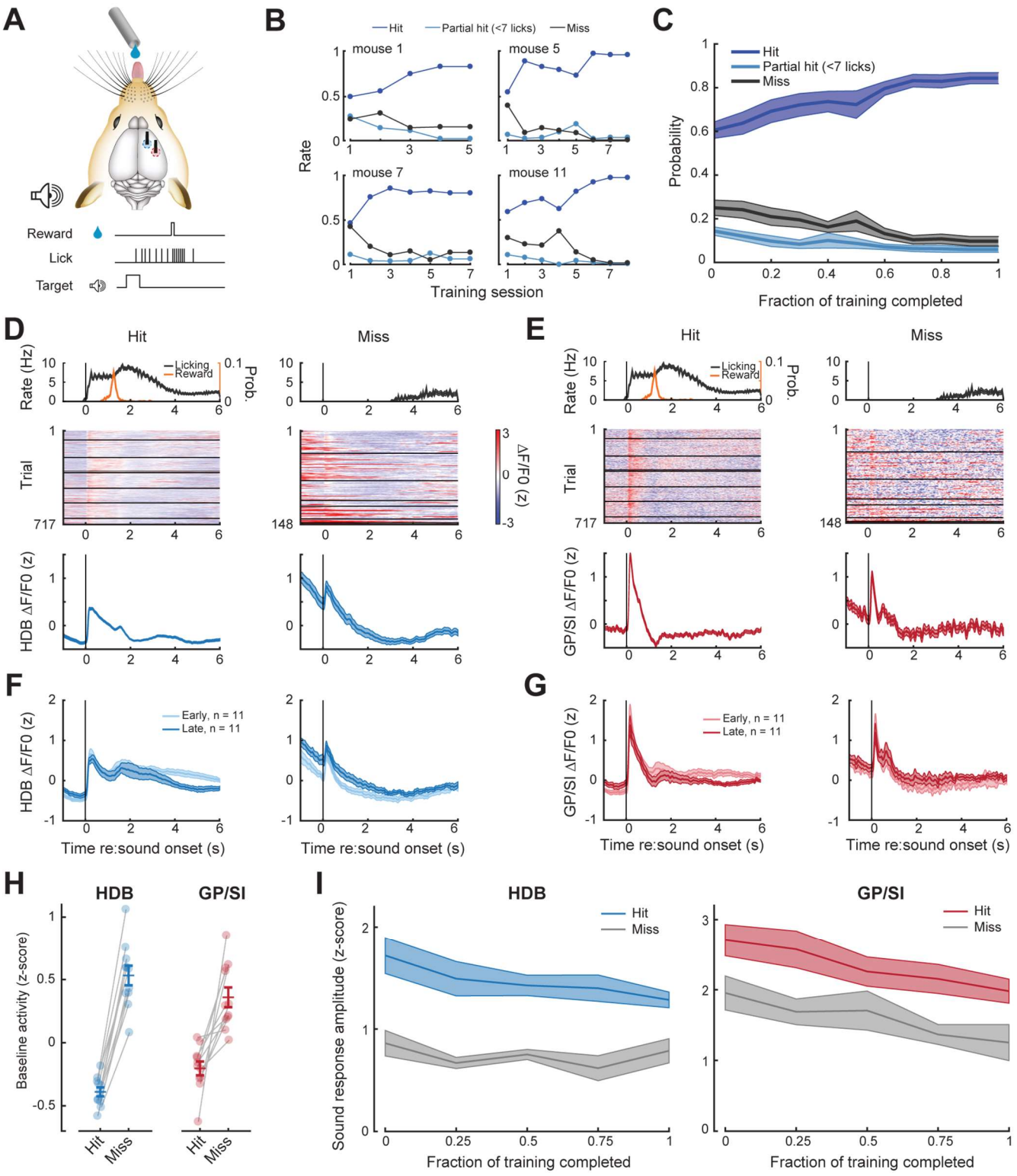

Figure 3. Pre-stimulus cholinergic basal forebrain activity distinguishes behavioral hit and miss trials during an auditory detection task.

(**A**) Mice were rewarded for producing a vigorous bout of licking (at least 7 licks in 2.8s) shortly after a low-, mid-, or high-frequency tone.

(**B**) Learning curves from four example mice that became competent in the detection task at slightly different rates.

(**C**) Mean ± SEM probability of hit, partial hit, and miss trial outcome as fraction of training completed in N = 11 mice.

(**D-E**) Tone-evoked cholinergic GCaMP responses from the HDB (*D*) and GP/SI (*E*) of a single mouse from 717 hit and 148 miss trials distributed over eight appetitive conditioning sessions. Left columns present the timing of lickspout activity, reward probability, heatmaps single trial fractional change values, and mean ± SEM fractional change values. Right columns present the same data on miss trials. Horizontal black lines in heatmaps denote different daily recording sessions. Vertical lines denote tone onset.

(**F-G**) Plotting conventions match *D-E*, except that data are averaged across all mice (N=11) and the first third of training trials (early) are plotted separately from the last third of training trials (late). No obvious training-related plasticity in the sensory-evoked responses were observed.

(**H**) Mean baseline activity during a 1s period preceding stimulus onset on hit and miss trials. Circles denote individual mice (N=11 for all conditions), bars denote sample mean and SEM. Pre-stimulus baseline activity was significantly higher on miss trials than hit trials, particularly in GP/SI (2-way repeated measures ANOVA with trial type and structure as independent variables: main effect for trial type, $F = 102.04$, $p = 1 \times 10^{-6}$; trial type × structure interaction, $F = 7.89$, $p = 0.02$).

(**I**) Mean ± SEM sound-evoked response amplitudes in all 11 mice were calculated by subtracting the mean activity during a 2s pre-stimulus baseline period from the peak of activity within 400ms of sound onset. Each post-reversal behavior session was assigned to one of five different discrete time bins according to the fraction of total training completed. Although sound-evoked responses are reduced on miss trials compared to hit trials, they remain relatively stable across all conditions as mice learn to associate neutral sounds with reward (3-way repeated measures ANOVA with training time, trial type, and structure as independent variables: main effect for training time, $F = 2.46$, $p = 0.08$; main effect for trial type, $F = 14.74$, $p = 0.012$; training time × trial type × structure interaction, $F = 0.56$, $p = 0.7$).

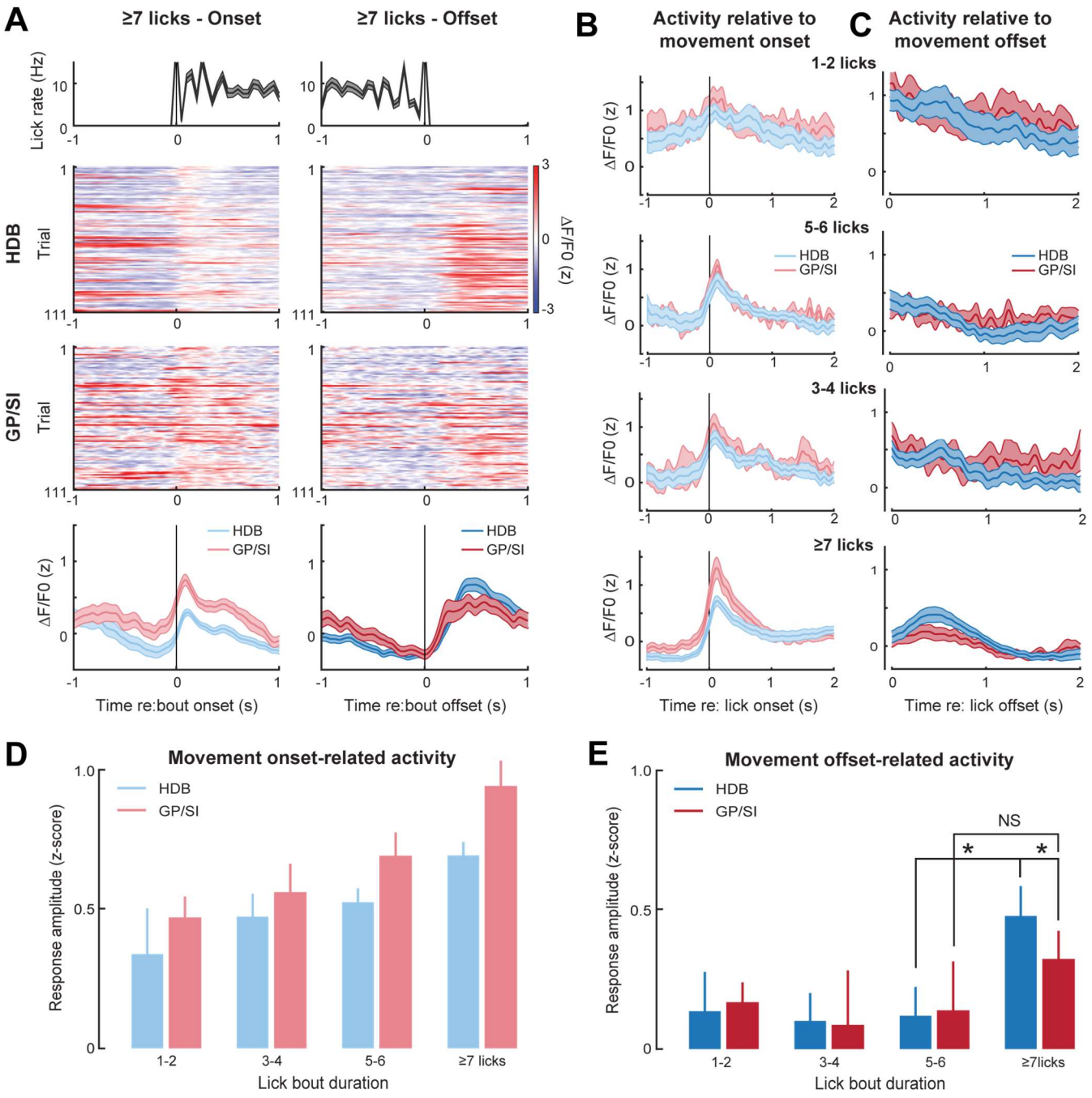

Figure 4. Motor-related activation of the cholinergic basal forebrain

(**A**) HDB and GP/SI activity from an example mouse related to the onset (left column) and offset (right column) of vigorous lick bouts during the inter-trial period of the appetitive operant task. Line plots in top and bottom row reflect mean ± SEM.

(**B-C**) Inter-trial lick bouts were binned according to whether they contained 1-2, 3-4, 5-6, or the full 7+ licks that would have produced reward delivery if produced at the appropriate time during the operant task. Mean ± SEM activity from N=11 mice related to the onset (*B*) or offset (*C*) of different lick bout durations.

(**D**) Response amplitudes related to lick bout onset were calculated by subtracting the maximum activity from the 250ms period preceding bout onset from the maximum activity occurring within 700ms following lickspout contact. Movement-related responses increased with lick bout duration and were greater overall in GP/SI than HDB (2-way repeated measures ANOVA with bout duration and structure as independent variables: main effect for bout duration, $F = 6.92$, $p = 0.001$; main effect for structure, $F = 6.33$, $p = 0.03$).

(**E**) Response amplitudes related to lick bout offset were calculated by subtracting the maximum activity from the 400ms preceding lick bout offset from the maximum activity occurring within 700ms following lick spout offset. Overall, the offset of licking did not elicit a response (2-way repeated measures ANOVA with bout duration and structure as independent variables: main effect for bout duration, $F = 1.47$ $p = 0.24$). In HDB, a response was observed at the offset of licking, but only for intense bouts of ≥ 7 licks (pairwise post-hoc contrast: 7+ vs 5-6, $p = 0.01$). No comparable response was observed in GP/SI (pairwise post-hoc contrast: 7+ vs 5-6, $p = 1$; 7+ GP/SI vs HDB, $p = 0.03$). Asterisks denote pairwise contrast p values < 0.05 after correcting for multiple comparisons. NS = not significant.

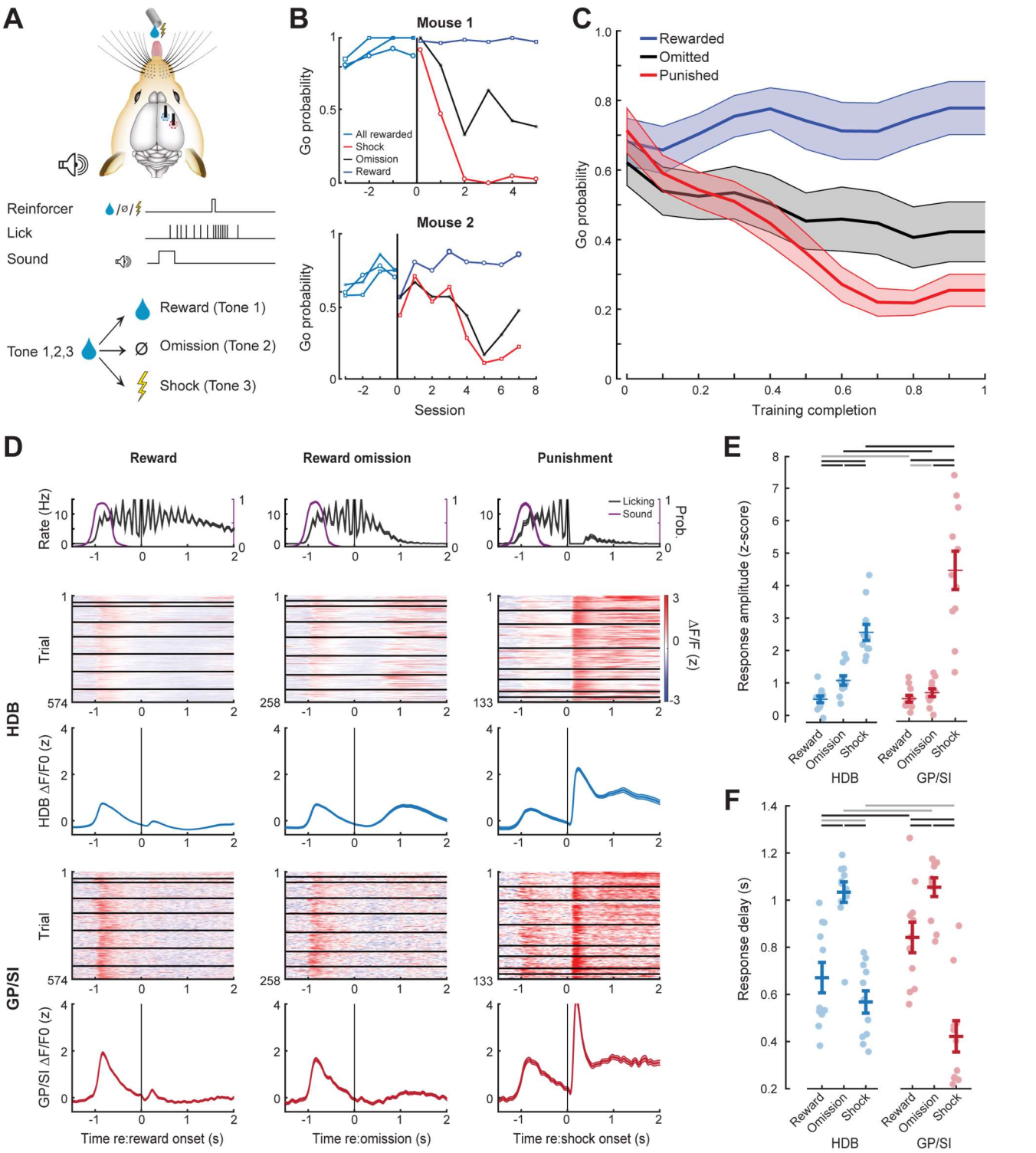

Figure 5. Differential activation of the rostral and caudal cholinergic basal forebrain in response to reward, punishment, and reward omission.

(**A**) Once mice were reliably licking for reward following the onset of the low- mid- or high-frequency tone, the reinforcement outcome was changed such that ≥ 7 licks in 2.8s elicited a tongue shock for one frequency and the omission of reward for the other.

(**B**) Go (≥ 7 licks in 2.8s) probability for all three tones when they were all associated with reward and after the reinforcement outcome was changed for two of the tones. Data are shown for two mice that modify they behavior to the change in reinforcement outcome at different rates. Vertical line denotes the transition from all rewarded to differential outcome. Circle, asterisk, and squares indicate low-, mid-, and high-frequency tones, respectively.

(**C**) Mean ± SEM Go probability for each reinforcement outcome as fraction of training completed in N = 11 mice.

(**D**) Tone-evoked cholinergic GCaMP responses from the HDB (*rows 2-3*) and GP/SI (*rows 4-5*) of a single mouse from 965 Go trials distributed over eight behavioral sessions following the change in reinforcement outcome. All data are plotted relative to reinforcement onset. *Top row:* Timing of lickspout activity (black) and tone onset probability (purple). *Rows 2 and 4:* heatmaps of single trial fractional change values in HDB (row 2) and GP/SI (row 4). Horizontal black lines in heatmaps denote different daily recording sessions. *Rows 3 and 5:* Mean ± SEM corresponding to each of the heatmaps above. Vertical lines denote reinforcement onset.

(**E**) Reinforcement-related response amplitudes were calculated by subtracting the mean activity during a 2s pre-stimulus baseline period from the peak activity occurring within 2s following the 7th lick. Circles denote individual mice (N=11 for all conditions), bars denote sample mean and SEM. Two-way repeated measures ANOVA with reinforcement type and structure as independent variables: Reinforcement type, $F = 80.62$, $p = 3 \times 10^{-10}$; Structure, $F = 5.7$, $p = 0.03$; Reinforcement type × structure interaction, $F = 8.01$, $p = 0.003$. Black and gray horizontal lines denote significant ($p < 0.05$) and non-significant pairwise contrasts after correcting for multiple comparisons.

(**F**) Reinforcement-related response latency were calculated by calculating the mean latency of the single trial peak responses relative to the offset of the 7th lick. Circles denote individual mice (N=11 for all conditions), bars denote sample mean and SEM. Two-way repeated measures ANOVA with reinforcement type and structure as independent variables: Reinforcement type, $F = 51.28$, $p = 1 \times 10^{-8}$; Structure, $F = 0.08$, $p = 0.78$; Reinforcement type × structure interaction, $F = 7.52$, $p = 0.004$. Black and gray horizontal lines denote significant ($p < 0.05$) and non-significant pairwise contrasts after correcting for multiple comparisons.

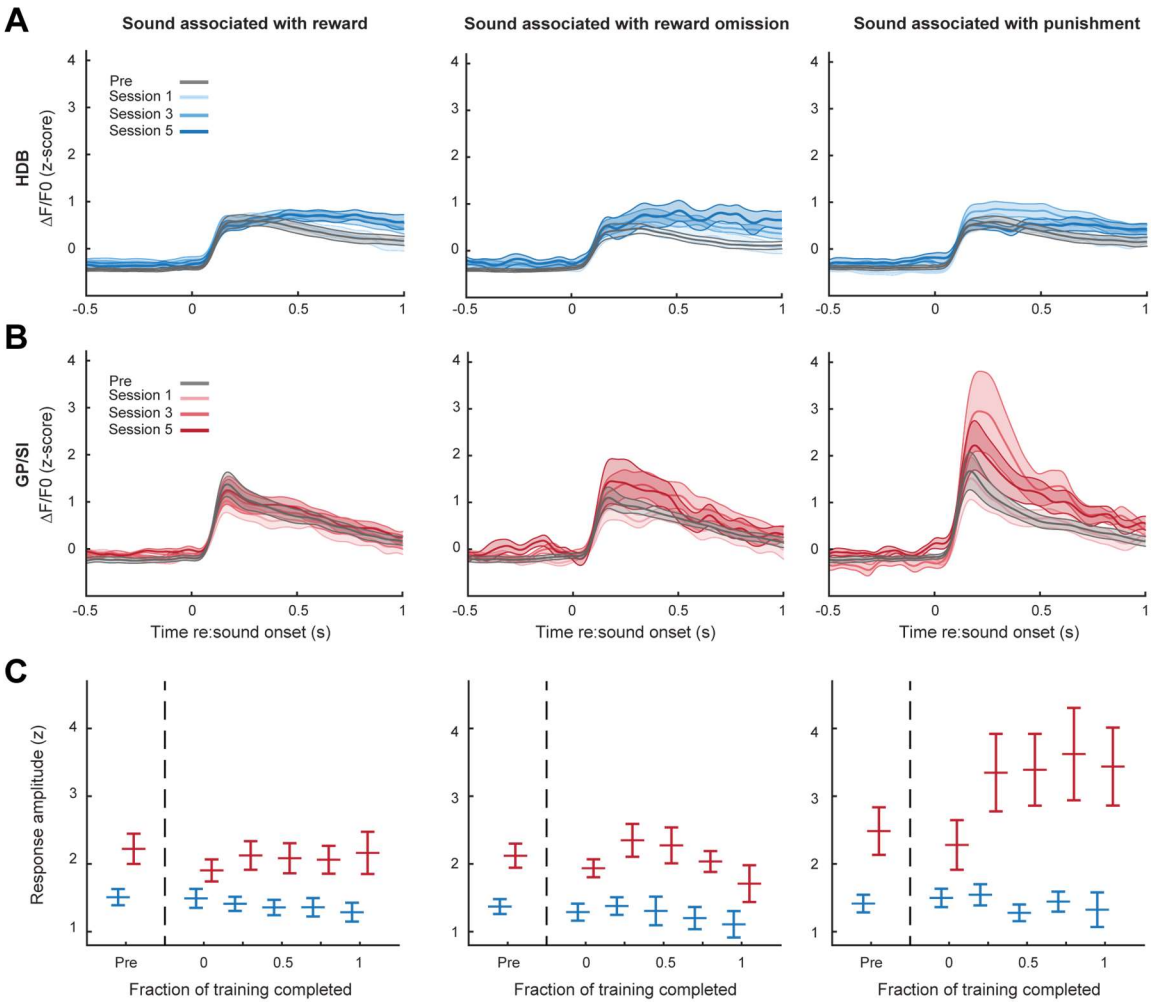

Figure 6. Learning-related enhancement of the auditory cue response is observed with aversive reinforcement, not reward, but only in GP/SI.

(**A-B**) Mean ± SEM tone-evoked GCaMP activity in HDB (N=11, *A*) and GP/SI (*B*) for the tone frequency associated with anticipated reward (left column), unanticipated reward omission (middle column) and punishment (right column) during the initial all-rewarded stage of training (gray) and at three sessions following the transition to the variable reinforcement outcome stage.

(**C**) Mean ± SEM sound-evoked response amplitudes in HDB (N=11) and GP/SI were calculated by subtracting the mean activity during a 2s pre-stimulus baseline period from the peak of activity within 400ms of sound onset. Each post-reversal behavior session was assigned to one of five different discrete time bins according to the fraction of total training completed. Sound-evoked responses were greater overall in GP/SI than HDB but were only enhanced during reversal learning for the frequency associated with punishment (3-way repeated measures ANOVA with training time, reinforcement type, and structure as independent variables: main effect for training time, $F = 1.62$, $p = 0.18$; main effect for reinforcement type, $F = 3.99$, $p = 0.03$; main effect for structure, $F = 23.38$, $p = 0.0006$; training time × reinforcement type × structure interaction, $F = 2.2$, $p = 0.04$).

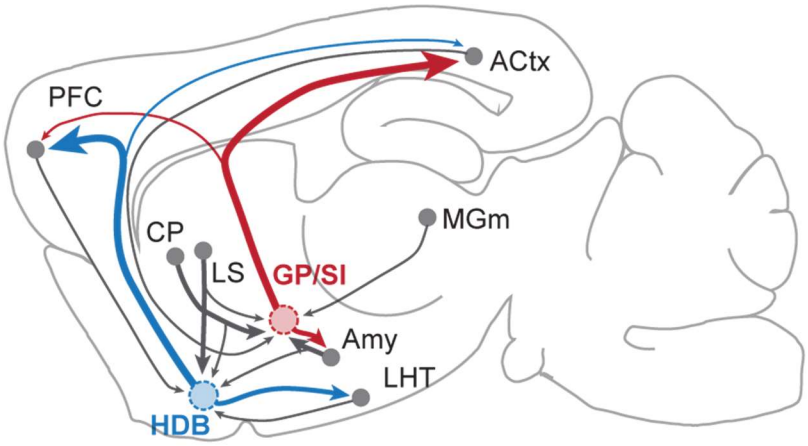

Experimental variable	Relative involvement
Pupil-indexed arousal (Fig. 1)	HDB > GP/SI
Predicting perceptual outcome (Fig. 3)	HDB > GP/SI
Reinforcement - reward omission (Fig. 5)	HDB > GP/SI
Passive sensory - auditory (Fig. 2)	GP/SI > HDB
Licking / Orofacial movement (Fig. 4)	GP/SI > HDB
Reinforcement - punishment (Fig. 5)	GP/SI > HDB
Learning-related sensory plasticity - punishment (Fig. 6)	GP/SI > HDB
Adaptation to stimulus novelty (Fig. 2)	Equivalently strong
Passive sensory - visual (Fig. 2)	Equivalently weak
Reinforcement - reward (Fig. 5)	Equivalently weak
Learning-related sensory cue enhancement - reward (Fig. 3)	Equivalently weak

Figure 7. Summary of functional specializations between the rostral and caudal basal forebrain. A summary of the relative involvement of HDB and GP/SI across all experimental variables tested here.

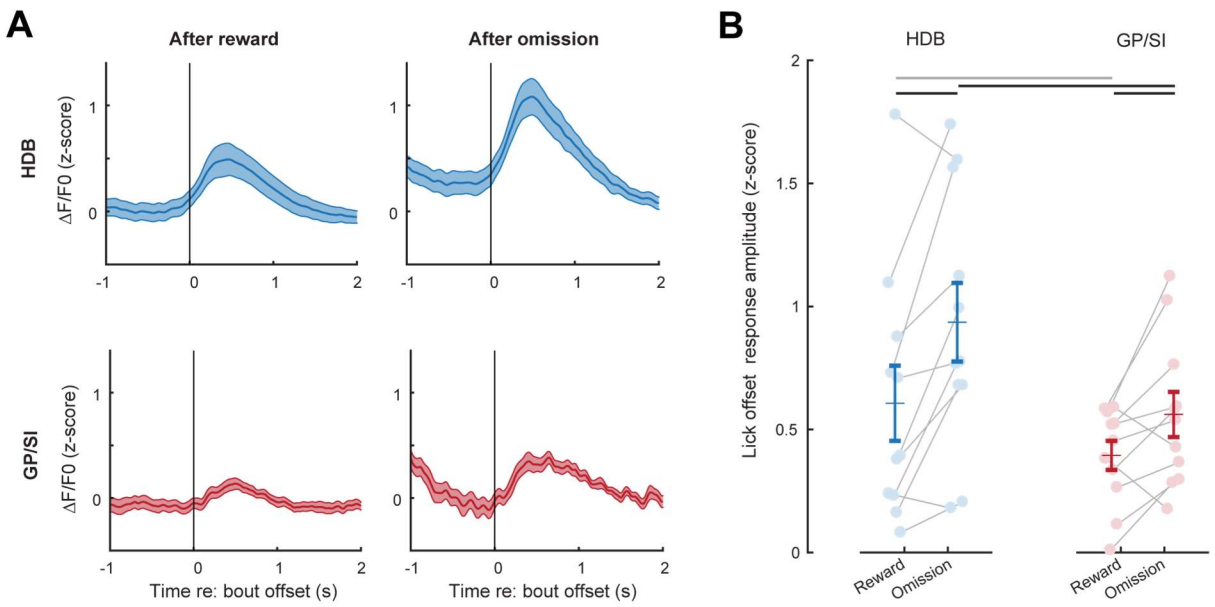

Figure 5 – figure supplement 1. Summary of functional specializations between the rostral and caudal basal forebrain.

(**A**) Mean ± SEM tone-evoked GCaMP activity in HDB and GP/SI (N=11 mice) relative to the offset of licking on rewarded (left column) and omission (right column) trials.

(**B**) Response amplitudes in reward and omission trials were calculated by subtracting the maximum activity from the 400ms preceding lick bout offset from the maximum activity occurring within 700ms following lick spout offset. Circles denote individual mice (N=11 for all conditions), bars denote sample mean and SEM. Lick bout offset responses were greater in HDB overall and significantly greater in omission trials than rewarded trials suggesting that they reflect reward prediction error and not a motor-related signal (2-way repeated measures ANOVA with trial type and structure as independent variables: main effect for trial type, $F = 10.97$, $p = 0.007$; main effect for structure, $F = 8.55$, $p = 0.02$. Black and gray horizontal lines denote significant ($p < 0.05$) and non-significant pairwise contrasts after correcting for multiple comparisons.